Interreg North-West Europe RAWFILL

Co-funded by the Walloon region

I1.2.2 Deliverable – Geophysical imaging pre-sampling report

(Meerhout andfill)

Date: April, 2019

SUBJECT:	WPI1 Report of pre-sampling geophysical investigation on pilot landfill 1		
☒ report	☐ information	☐ consideration	☐ decision
To: …		From: BGS & Université de Liège	

Introduction

The following report describes the results of the first geophysical investigation on the former landfill of Meerhout, located in the province of Antwerp, Flemish Region, Belgium. This landfill is one of the main RAWFILL pilot sites to demonstrate the use of geophysical methods as part of a standard framework assessment of enhanced landfill mining projects.

In this initial survey, we applied a variety of complementary geophysical methods. The goal was firstly to delineate major geophysical anomalies, which are indicative for structural or compositional changes within the landfill or the transition to the host material. Secondly, it allows identifying ideal sampling locations in order to verify and calibrate the geophysical measurements. Based upon the outcome of this survey the Public Waste Agency of Flanders (OVAM) will conduct a guided sampling survey. Identified correlations between geophysical results and ground-truth data may be useful for subsequent characterization of other landfills with geophysics. Furthermore, depending on sampling results, a second geophysical survey might later be conducted to remove uncertainties issued after sampling.

The initial investigations were completed by the University of Liege (Liège) and the British Geological Survey (BGS) on January 15-18, 2018. They were prepared in close coordination with OVAM and the members of the IOK (owner of the site) and based upon 1) the expected outcome of geophysical methods for LF characterization presented in the SWOT analysis and 2) the information gathered in the archives of the Meerhout site (see T1.3.1: Swot analysis of LF characterization methods, I1.1.1: Archives and inventory report and I1.1.2 Remote imaging report). A detailed description of the survey design can be found in the Survey Design Report (D I1.2.1). Although, the actual investigations were slightly adjusted according to site conditions and work progress.

Summary of the study area

The Meerhout landfill was developed in five stages since 1962 until 1997. As shown in Figure 1a, five different zones were filled during the first four stages between 1962 and 1989. During the last stage from 1993 to 1997 an additional layer of waste was added on top of the zones 4 and 5. This development lead to a different waste thickness from 5 m in zone 1 to 20 m in zones 4 and 5. During the first stage of the landfill, no bottom membrane was set up whereas in more recent periods, an agricultural foil (1982-1983) and a high-density polyethylene (HDPE) membrane (>1986) were used. Although, the location of the agricultural foil remains unclear.

Information about the waste composition during the first stage is missing. According to available information from 1981 to 1997, at least 1.3 million m^3 of household and industrial (up to 30%) wastes were deposited on the site.

From 1999 to 2003, gas was extracted from the landfill through nine wells distributed all over the landfill. During that period, the average annual gas production amounted to 376 000 m^3.

At present a low amount of gas is extracted and burnt for one hour every day. The oldest and easternmost part of the landfill is now paved with cement and acts as a recycling park.

Further details about the study site can be found in the following reports: I1.1.1: Archives and inventory report & I1.1.2 Remote imaging report.

Geophysical investigations

Main investigation areas

For the geophysical survey, we focused on the two investigation areas shown in Figure 1b. These two areas were chosen because they are representative for the different stages of the landfill exploitation. Additionally, the lack of dense vegetation cover on these areas facilitated detailed geophysical mapping.

The northern investigation area 1 (yellow in Fig. 1b) covers the older parts of the landfill and extends across three filling-zones. In this part, the waste reaches a thickness of 8 to 10 m with a potentially higher amount of industrial waste. The newer, southern investigation area 2 (blue in Fig. 1b) in contrast, has a waste thickness of approximately 20 m potentially containing intermediate layering. Additionally in area 2, an intact HDPE membrane is present whereas in area 1 only a probably by now degraded agricultural foil was used for sealing. For the geophysical measurements, the possibilities and challenges are thus different for the two investigation areas. In addition, it should be noted that ERT and IP measurement can only be conducted on investigation area 1 since the waste material on the other parts is completely electrically isolated by the HDPE membrane and therefore invisible to this measurement method.

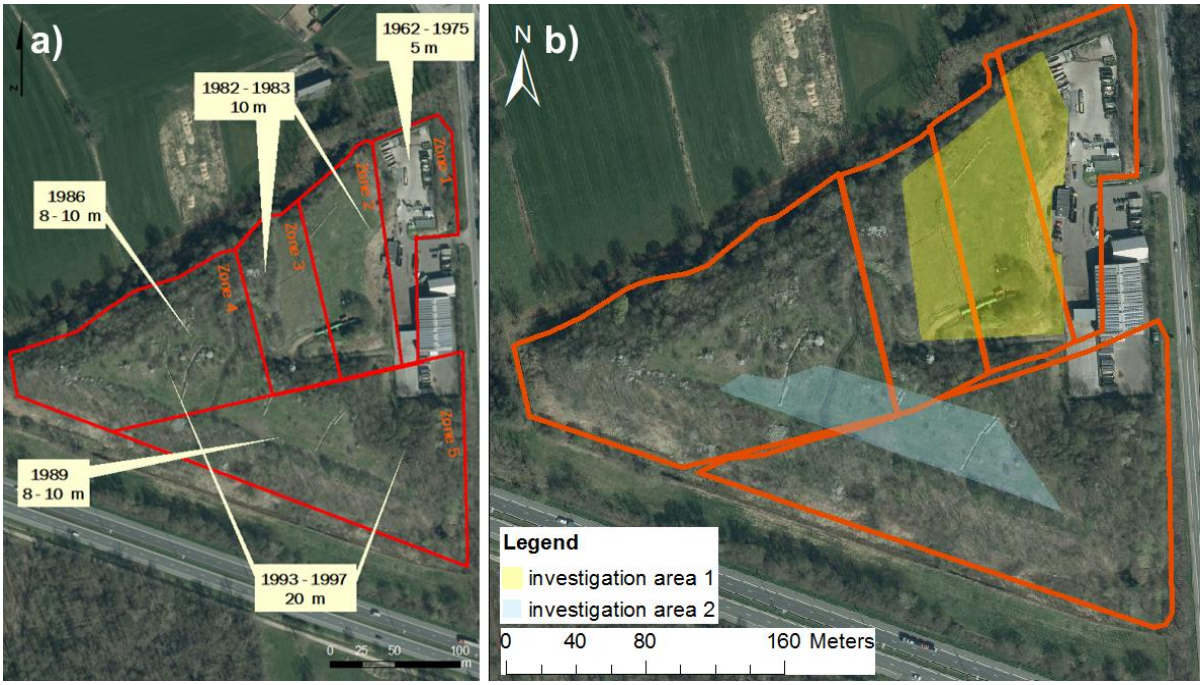

Figure 1: Aerial view of Meerhout landfill with a) site history with estimated waste thickness and b) extent of the initial pre-sampling geophysical survey (aerial photograph taken in 2017).

Geophysical methods and coverage

In the following, all applied geophysical methods are listed with their expected main sensitivities on landfills. Different geophysical methods are sensitive to different physical properties and can therefore complement each other. For a more detailed description of each geophysical method, please refer to the following report T1.3.1: Swot analysis of LF characterization methods.

In order to get a full areal coverage the following mapping methods were used:

- **Magnetic field mapping:** to identify zones with high metal content (measuring changes in total magnetic field/gradient)
- **Electromagnetic (EM):** to reveal lateral extent of different waste composition or leachate content at several distinctive depths (mapping changes in electrical conductivity and magnetic susceptibility)

More focused 2D surveys, providing detailed information about changes of physical properties with depth, were done along distinct profiles including the following methods and their sensitivities:

- **Electrical Resistivity Tomography (ERT):** to discriminate different waste types and investigate changes in leachate content (measuring resistivity distribution)
- **Induced Polarization (IP):** to detect metallic scraps or zones of higher organic content (measuring chargeability distribution)
- **Seismic Refraction Tomography (SRT) and Multichannel Analysis of Surface Waves (MASW):** to characterize the geometry of the subsurface layers presenting different compactions (measuring seismic velocities)
- **Horizontal to Vertical Noise Spectral Ratio (HVNSR):** to estimate the thickness of the landfill (measuring seismic velocities)
- **Ground Penetrating Radar (GPR):** to indicate the presence of a covering membrane (registering the returned GPR signal which was reflected or diffracted at material boundaries with significant changes in relative electric permittivity)

The extent of each applied method is shown in Figure 3. The EM and magnetic mapping were performed on a grid, formed of parallel lines (yellow and blue dots in Fig. 3a). The 2D surveys were done along the profile lines indicated in Figure 3b. As mentioned above, the ERT and IP methods could only be applied on the northern area where no covering membrane is present. Due to a lack of time, the application of GPR was limited to the northern area along the northernmost, easternmost and westernmost profiles.

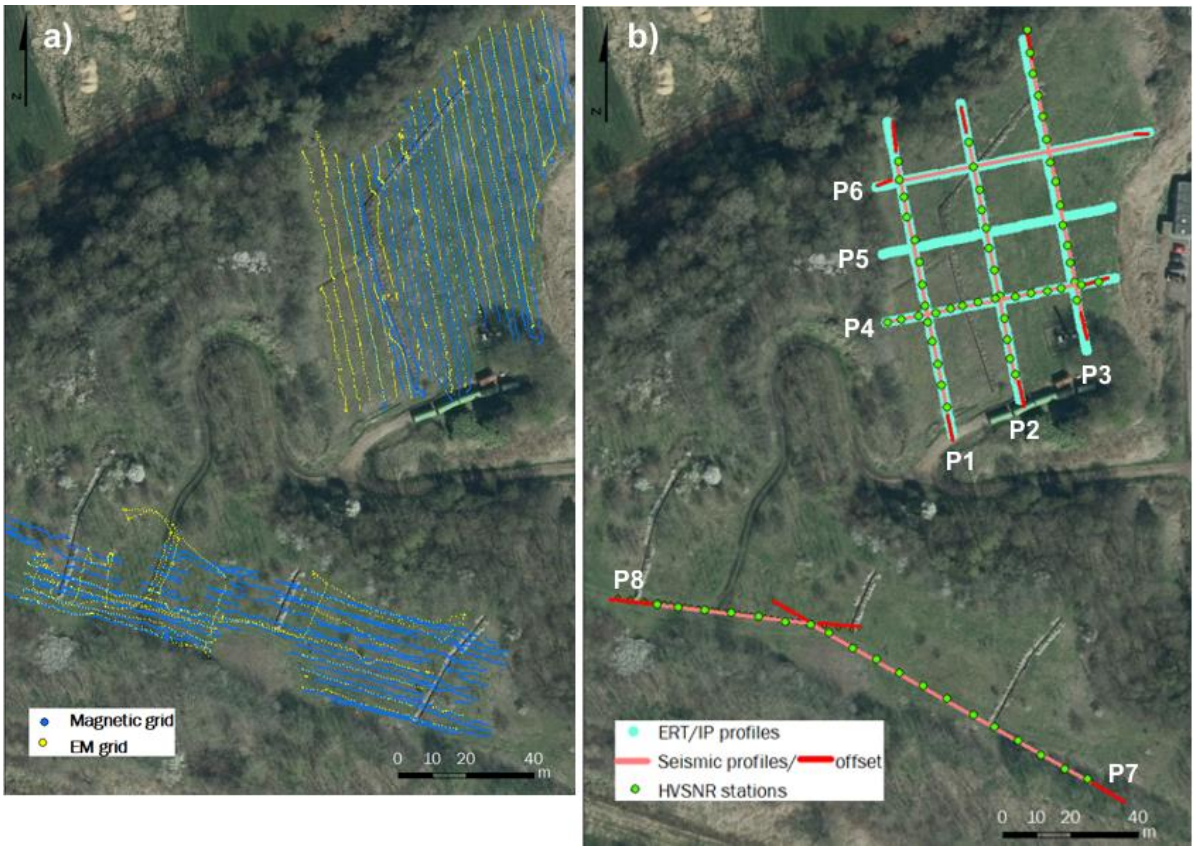

Figure 2: Extent of the performed geophysical measurements. a) Electromagnetic (yellow) and magnetic (blue) survey grid. Line spacing of 4 and 2 m respectively. b) Location of ERT/IP profiles (thick green lines in the bottom part of the site). Seismic profiles (pink lines) with offsets indicated by red lines at the beginning/end of each profile. Location of HVSNR seismic station is shown in green dots distributed along seismic profiles.

Measurement systems and parameters

In the next section, the measurement parameters for each method are summarized. A summary table with more detailed additional information can be found in appendix A.

The **electromagnetic** data was acquired using a conductivity meter model DUALEM-4. By attaching two different antennas sizes, mapping at four different depth levels could be achieved. These depths were 1.2 m and 3 m for the shorter antenna and 2.5 m and 6 m for the longer antenna. Both quadrature (related to apparent conductivity) and in-phase (related to apparent magnetic susceptibility) components were recorded simultaneously for each antenna. In addition, a GPS sensor (no RTK) was connected to the system for positioning. The EM survey for the northern area was conducted on a grid of 4 m spaced lines for the larger antenna and 2m spaced lines for the shorter antenna (yellow dots of Fig. 3a). For the southern area, the acquisition lines are more irregular due to the parts of denser vegetation cover. The EM system was mounted to a cart as shown in Fig. 4a.

The **magnetic** data were acquired with a portable caesium magnetometer model G-858 from Geometrics. All data were recorded in vertical gradient mode with 1 m separation between sensors and 0.6 m above ground level. The system was mounted on a cart as shown in Figure 4b. Lines interspacing for the northern grid was approximately 2 m (see blue dots Fig. 3a). For positioning, all data were continuously synchronized with a GPS system (no RTK). To identify drifts in the magnetic data the repeated base measurements were done at a position away from any visible disturbances.

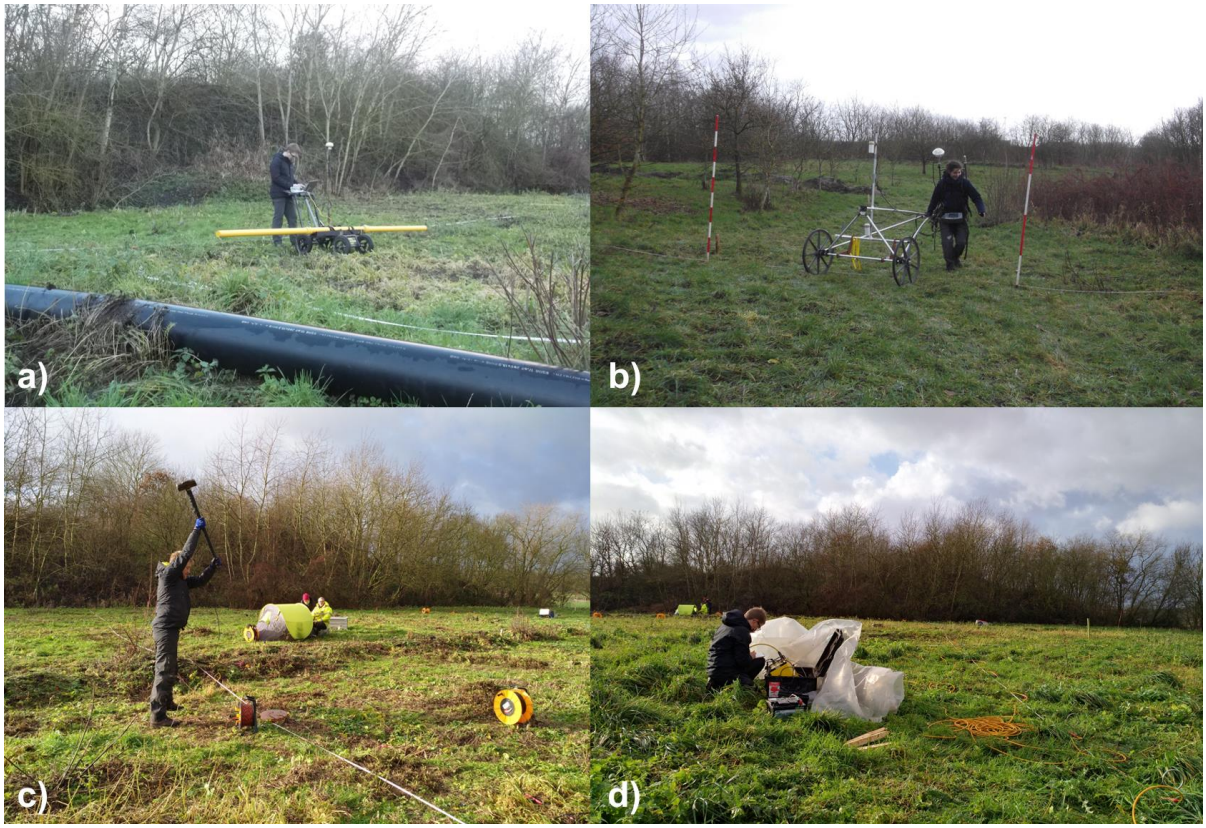

Figure 3: Acquisition of a) EM, b) Magnetic, c) Seismic (SRT and MASW) and ERT/IP data on the landfill.

ERT and time-domain IP data were simultaneously recorded with a SuperSting R8/IP system. The electrode spacing was 1.5 m leading to an approximate resolution of 0.4 m in profile direction. The resolution in vertical direction decreases with depth ranging from 0.4m at depth up to 1.4 m to 0.8 m at depth up to 6 m and 1.5 m at maximum investigation depth. The maximum investigation depth achieved was 12 – 15 m depending on the profile length, which varied from 69 to 94.5 m due to topography and vegetation barriers. For each profile, a set of 1100 to 1800 reciprocal dipole-dipole configuration pairs were measured. This setup allowed a good data coverage and the reciprocal errors could be used for data quality assessment. Finally, each electrode was surveyed with a differential GPS with real time kinetic (RTK) corrections for accurate positioning of the profiles.

The seismic data were acquired with densely spaced shot locations (every other geophone). This allowed us to use the data for both **Seismic Refraction Tomography (SRT)** and **Multichannel Analysis of Surface Waves (MASW)** data processing. All data were acquired with vertical geophones. For some lines, 4.5Hz and 10Hz geophones were used interchangeably. The maximum investigation depth for MASW is considered to be about half of the wavelength of the lowest recorded surface wave frequency (e.g Park, Miller et al. 1999, Dumont, Robert et al. 2017). Meaning that with lower frequency geophones the investigation depth for MASW can be increased. Since only a limited amount of lower frequency geophones was available, we decided that the interchangeable use of 4.5 and 10 Hz geophones was the best trade-off in order to contemplate the investigation depth for SRT, which is about 5 to 10 times smaller than the profile length (Knödel, Lange et al. 2007). Due to the larger waste thickness on investigation area 2, we used a geophone spacing of 2 m. On investigation area 1, the profiles were acquired with different geophone spacings ranging from 1.25 to 1.6 m because profile length limitations caused by topography and vegetation. As a source, a sledgehammer and a plastic plate were used as shown in Figure 4c. For positioning, each geophone was localized with a differential GPS (with RTK corrections).

The method of **horizontal to vertical noise spectral ratio (HVNSR)** was applied along the seismic profile lines by recording ambient seismic noise during 15 minutes at discrete locations. Data were recorded in the three components (vertical, north-south, east-west directions) using two seismometers LE-3Dlite MkIII and LE-3D/5s MkIII, with eigenperiods of 1s and 5s and upper frequency limit of 100 Hz and 50 Hz respectively. Each measurement location was separated by a distance of four previously positioned geophones. The recording stations alternated between both seismometers.

The **ground penetrating radar (GPR)** was used to check the presence of a covering membrane in area 1 and to estimate the cover layer thickness. Three profiles were measured with a 250MHz antenna, which represents the best compromise between depth of investigation (to detect the covering membrane) and resolution (to estimate the cover layer thickness).

Geophysical processing and results

The processing of data and results of each geophysical method is described in the following section. The section concludes on discussing the overall interpretation with respect to the landfill characterization and the suggested sampling locations. Proposed sampling locations are indicated in presented maps and discussed in the concluding section.

Magnetics

Figures 4 and 5 display the results of the total magnetic survey. As described in the previous section, the magnetic data were acquired with two vertically aligned sensors, whereas both sensors measure the total magnetic field (in nT). The map in Figure 4 displays the data measured with the lower sensor after applying a spatial interpolation with inverse distance weighting (IDW). The normal magnetic field intensity at the landfill site is about 48842.9 nT (taken from IGRF online tool which takes into account the latitude, longitude and elevation of the site). Therefore, the blue and red colours on the map in Figure 4 correspond to magnetic anomalies.
The vertical gradient map in Figure 5 is obtained by calculating the difference of the total magnetic field measured at the two sensors and interpolating the data using IDW. Especially for landfill studies, the vertical magnetic field gradient offers several advantages. Firstly, it is more sensitive to near-surface anomalous magnetic sources. Secondly, due to the signal subtraction, unwanted signal perturbation such as the influence of temporal variations of the total magnetic field and the influence of the earth magnetic field inclination, can be reduced (e.g. Roberts et al. 1990a and Roberts et al. 1990a).

Several very strong magnetic anomalies are seen on both Figures 4 and 5, which can be associated with metallic infrastructure or obstacles disturbing the measurements. The investigation area 1 shows a relatively big, rotated L-shaped structure running parallel to the access road (white dashed lines in Fig. 4 & 5). Due to its elongated and continuous shape we assume that this feature is caused by a metallic pipe. Similarly, a very high amplitude anomaly can be seen at the southern edge of this area. This anomaly can be associated to the metallic containers nearby. On investigation area 2, several high amplitudes, North-South aligned anomalies are present. These structures are in line with trenches on this area and were probably caused by tilting of the sensors when crossing the trenches (indicated by black arrows in Fig. 4 & 5). Another big anomaly close to the proposed sampling location 10 can be associated to a metallic borehole casing at this position (black cross in Figs. 4 & 5).

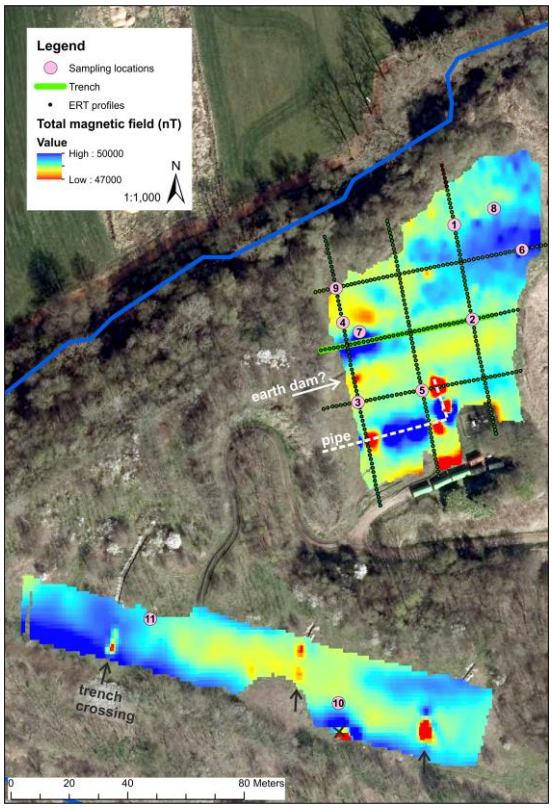

Figure 4: Total magnetic field map

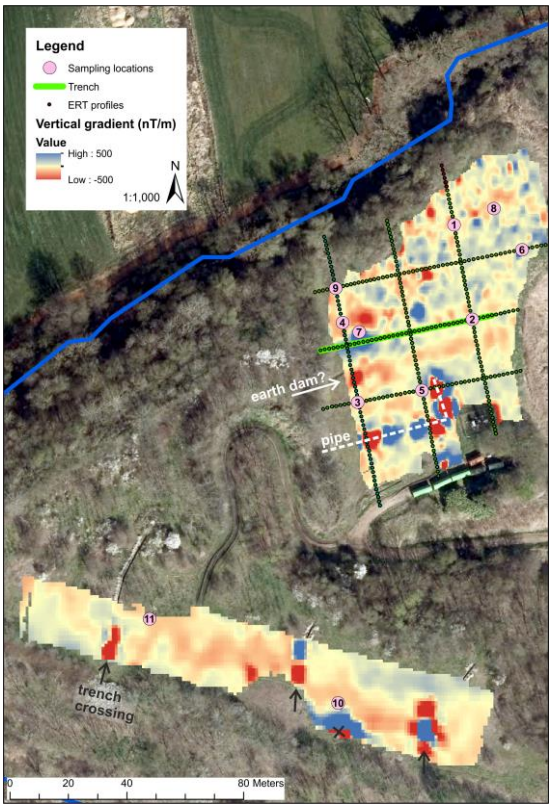

Figure 5: Vertical magnetic gradient map

The total magnetic data shows very broad magnetic anomalies. The broad shape might be an indication for compositional changes at greater depth within the waste material or even changes in the underlying geological structure. The narrow structure near the proposed sampling location 7, in contrast, might be caused by a bigger metallic object at shallow depth.

In comparison to the total field measurements, the magnetic gradient data is much more perturbed with values fluctuating from negative to positive (fig 5). This is especially true for the north-eastern part of investigation area 1. Such fluctuating values are a typical observation for landfills due to their high concentration of ferromagnetic material and is described for example in Knoedel et al. (2007). The values in area 2 are in comparison much less fluctuating indicating a lower amount of ferromagnetic material in this newer part of the landfill.

Another pronounced feature crosses the center of the investigation area 1 in East-West direction. Although, the waste cells are north south aligned (Figure 1), we wonder if this structure might be associated with an earth dam dividing waste cells (white arrow in fig 4 & 5).

Electromagnetic mapping

Similar to the magnetic data, all data were interpolated with IDW to produce maps. The quadrature-phase component of the induced magnetic field can be related to the electrical conductivity and the in-phase component to the magnetic susceptibility (e.g. Dumont et al. 2017). The data is sensitive to different depths depending on the antenna used, either 2 m or 4 m antenna, and the orientation of the coils. All maps with the conductivity data at four different depths are displayed in Figures 6 to 9. All magnetic susceptibility data are shown in Figures 10 to 13.

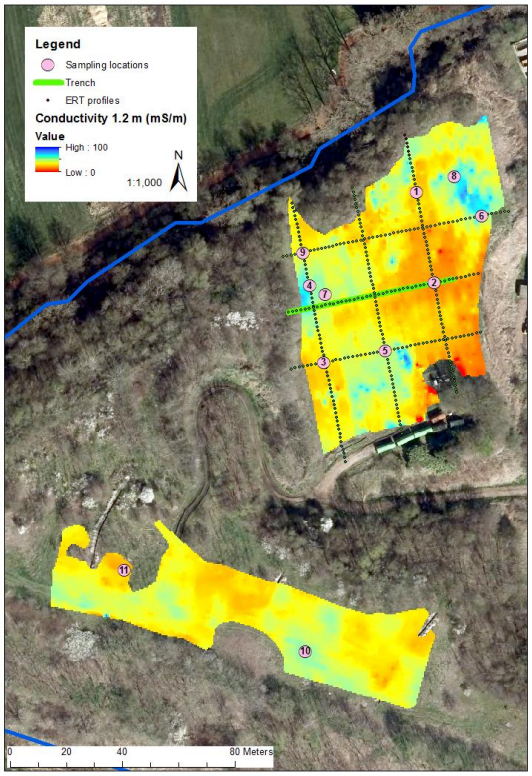

Figure 6: Electrical conductivity map derived from the quadrature-phase data measured with the 2 m antenna and vertical coil alignment. Investigation depth is 1.2 m.

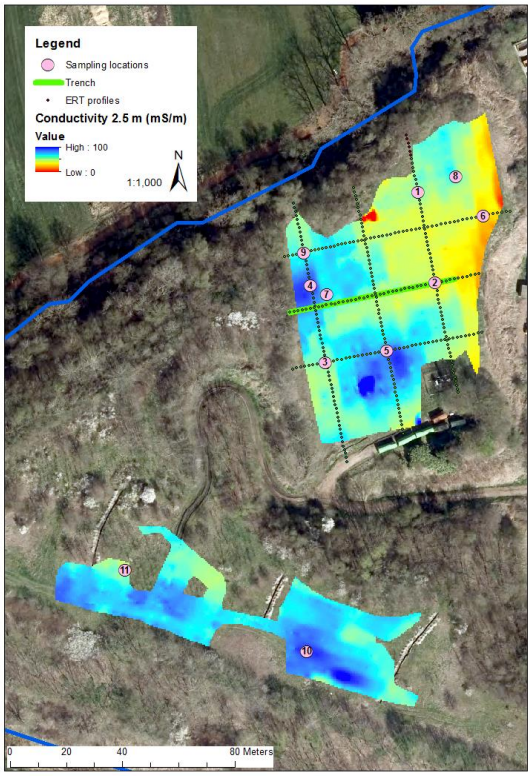

Figure 7: Electrical conductivity map derived from the quadrature-phase data masured with the 4 m antenna and vertical coil alignement. Investigation depth is 2.5 m.

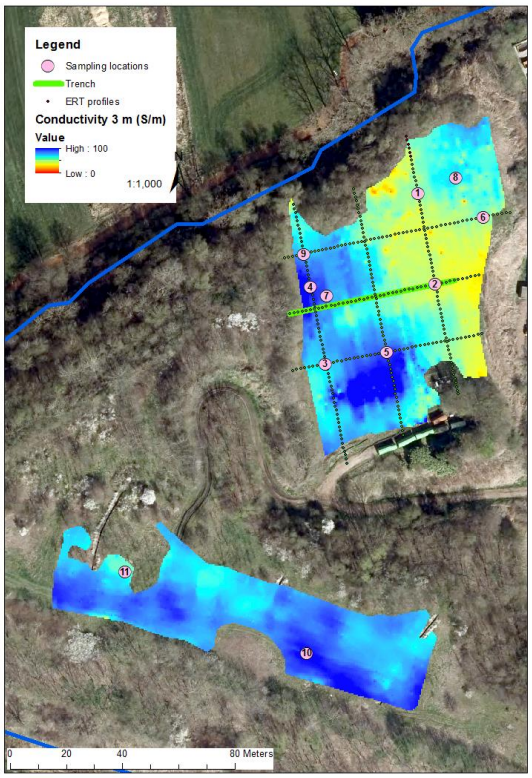

Figure 8: Electrical conductivity map derived from the quadrarture-phase data masured with the 2 m antenna and horizontal coil alignement. Investigation depth is 3.0 m.

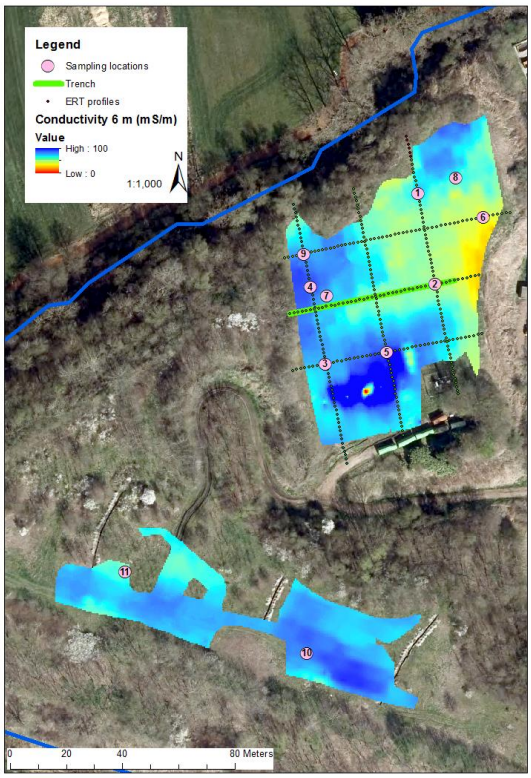

Figure 9: Electrical conductivity map derived from the quadrature-phase data masured with the 4 m antenna and horizontal coil alignement. Investigation depth is 6.0 m.

Figure 10: Magnetic susceptibility map derived from the in-phase data masured with the 2 m antenna and vertical coil alignement. Investigation depth is 1.2 m.

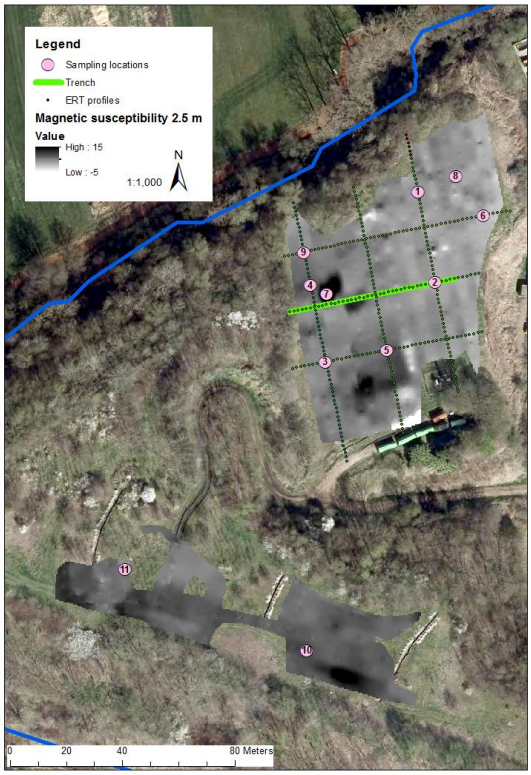

Figure 11: Magnetic susceptibility map derived from the in-phase data masured with the 4 m antenna and vertical coil alignement. Investigation depth is 2.5 m.

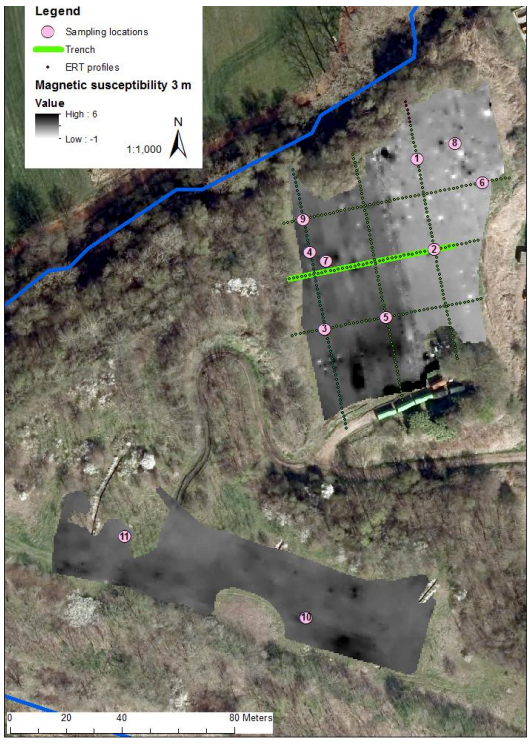

Figure 12: Magnetic susceptibility map derived from the in-phase data masured with the 2 m antenna and horizontal coil alignement. Investigation depth is 3.0 m.

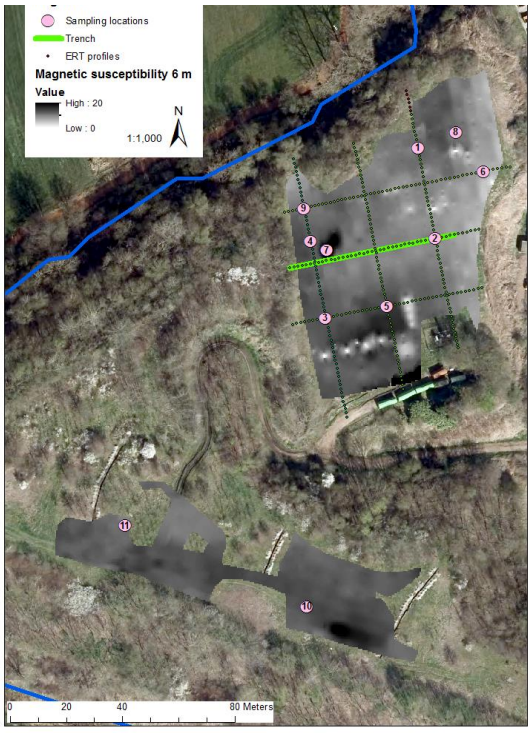

Figure 13: Magnetic susceptibility map derived from the in-phase data masured with the 4 m antenna and horizontal coil alignement. Investigation depth is 6.0 m.

Overall, the conductivity data show a clear increase with depth. Especially at 1.2 m depth (fig 6), the conductivities are significantly lower compared to the other measured depth (Figs. 7 to 9). This could indicate that the thickness of the cover layer must be very close or bigger than 1.2 m. The higher conductive patches seen on the map in Figure 6 could be caused either by a thinner cover layer or by a different composition of the cover layer or the immediately adjacent waste material. At the following depths, the same areas with higher conductivities persist and get more pronounced with depth. Compositional changes that can be associated with an increased conductivity could be: higher leachate content, higher amount of organic or metallic material or a higher clay content.

In the magnetic susceptibility data, it can be noted that the amplitudes are offset at certain parts of the maps. Especially in Figures 10 and 12, a clear shift is seen between the eastern and the western half of investigation area 1. We assume that this shift was caused by a drift of the measurement system since the measurement system was restarted before measuring the western half of the area. Equally, the values measured with the 4 m antenna are slightly offset. We limit the interpretation therefore to relative changes and the maps from Figures 10 – 14 are displayed with different amplitude ranges to enhance the visibility of relative changes.

On investigation area 1, the magnetic susceptibility indicates the presence of a metallic pipe. This is consistent with the observation made with the magnetometer. Equally, a pronounced anomaly is visible near sampling position 7, indicating a relatively big metallic object within the waste material located at a depth between 2.5 and 6 m. In addition, similar to the magnetic vertical gradient map, the data in the north-eastern corner is highly fluctuating, indicating a higher metallic content. Interestingly, this north-eastern area with a potential higher metal content is not represented with an area of significantly higher conductivities in Figures 7 to 9. This could have a structural explanation such as the presence of isolated metallic objects rather than an evenly distributed higher amount of metal. Alternatively, it could have a compositional explanation such as a comparable lower leachate, organic material or clay content. All of the latter would have no influence on the magnetic data but would decrease the measured conductivities.

On investigation area 2, it is again interesting to see that the magnetic susceptibility data do not show such pronounced anomalies as those observed in the total magnetic field data in Figure 4. This indicates that the changes in the total magnetic field data might be related to a change in the underlying host material or to compositional changes at larger depth than 6 m, which is the maximum investigation depth of the EM system.

Electrical resistivity tomography / IP

In a first pre-processing step the data were filtered for bad readings.
Individual readings were rejected if:

- Reciprocal errors of resistance (ERT) > 5%
- Standard deviation of repeat measurements > 2%
- Reciprocal errors of chargeability (IP) > 30%
- Voltages < 0.5 mV

With these processes 10.5% to 21.5% data points were deleted for each profile. The deleted data points correspond mainly to the deeper levels. This led to a slight reduction of the investigation depth but data coverage at the other levels is still ensured. Afterwards, the filtered ERT and IP data was inverted with the software Res2DInv (Loke 2016). All inversions converged within 5 to 7 iteration steps to a low RMS error below 3.5%. It must be mentioned here, that the easternmost IP profile P1 was measured with a longer time window (see appendix A). This could have partly caused the significant higher chargeability values of P1.

The inverted resistivity and IP profiles are displayed in Figure 14. A figure listing all profiles in 2D is shown in Appendix B and C.

In general the resistivity structure of the profiles verifies that no completely electrical isolating HDPE membrane is present. Otherwise, lower resistivity values at depth would not have been able to be detected.

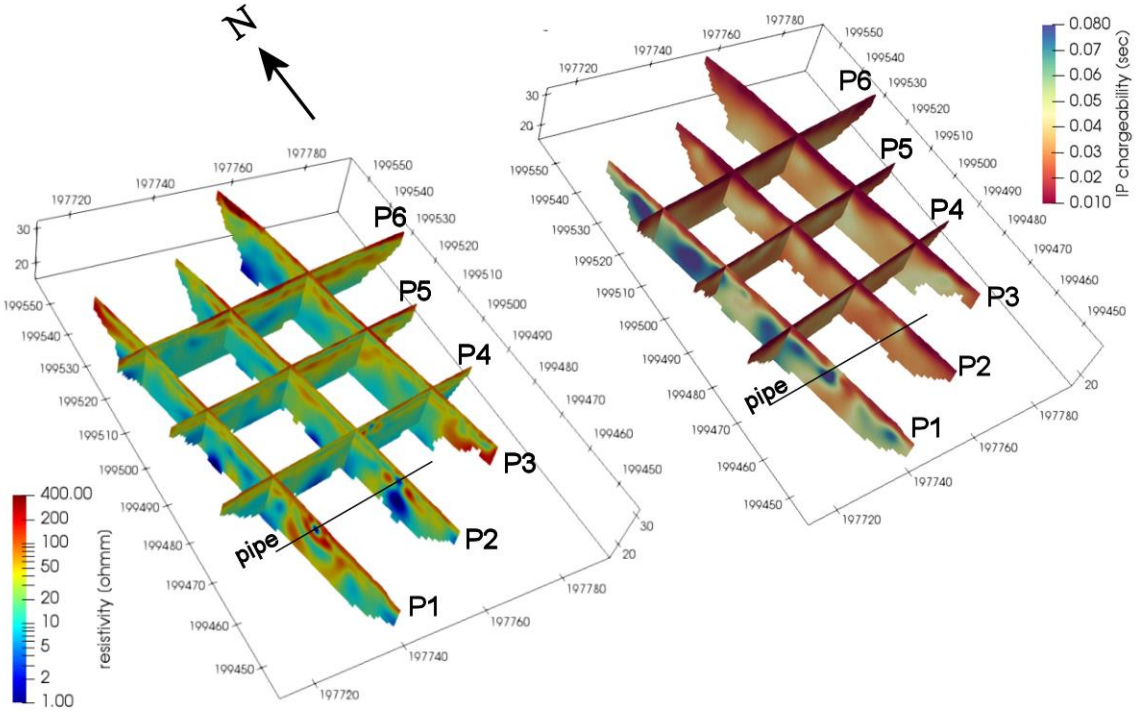

Figure 14: Inverted Electrical resistivity (left) and IP (right) profiles. The black line indicates the position of a metallic pipe.

In terms of infrastructure, again a very clear indication of a metallic pipe is seen in the southern half of the resistivity profiles P1 and P2 (see Fig. 14 and circle in Appendix B and C). This is consistent with the observations made in the magnetic and the EM (magnetic susceptibility) data. Equally, the general decrease in resistivity with depth is consistent with the conductivity measured with the EM system.

The first 4 to 6 m in the resistivity profiles show an interesting layered structure with a higher resistivity layer at the top, followed by a lower resistivity layer and then again a higher resistivity layer with slight lateral variations. Moreover, the higher resistivity layers are thicker towards East on profiles P5 and P6. This is again consistent with the EM data, which show a less conductive anomaly at the area around the eastern half of these two profiles. A similar observation can be made on the chargeability data, which show a layer of lower chargeability with a thickness generally decreasing towards West. Interestingly, the deeper boundary of this lower chargeable layer matches approximately the top boundary of the deeper, less resistive layer described above (compare black dotted lines in Appendix B and C). In general, a high chargeability is observed in landfills. This can be due to the presence of metal scraps, an increased organic material content (e.g. Angoran 1974; Aristodemou and Thomas-Betts 2000), wood content (Thierry et al., 2001) or the layering of plastic sheets that would act as electric capacitors (Carlson et al., 2001). Thus it is likely that the lower chargeability corresponds either entirely to the cover layer or it could also correspond to both the cover layer and a top layer of waste which has a different composition (e.g. more inert material) than the deeper adjacent waste layers. Similarly, from the ERT data we cannot be sure which boundary of the layered structure corresponds to the cover layer. Either it would be likely to be the thin, top resistive layer with a thickness of 1 to 2 m or the lower resistive second layer could correspond to a clay capping within the cover layer. The

bottom boundary of the deepest resistive layer could for example be caused by an increased amount of leachate content. To be sure about the correct interpretation, ground truth from the boreholes will be required.

Patches of lower resistivity or higher chargeability below the layered structure described above could again be caused by a locally different waste composition.

Ground penetrating radar

The ground penetrating radar data was processed with the software ReflexW from K. Sandmeier.

The radargrams were mainly analysed to find an indication about the presence of a geo-membrane and to detect the cover layer thickness.

Figure 14 displays in the background the radargram of the three measured lines. The ERT data is over-laid in the foreground of P3 and P1. Especially for lines 1 and 3, an indication of a boundary with a sharp change in electrical permittivity is detected and is comparable to the lower boundary of the top high resistivity layer in the ERT profiles. Such a change in electrical permittivity could indicate the change to either an underlying layer with higher clay or higher leachate content.

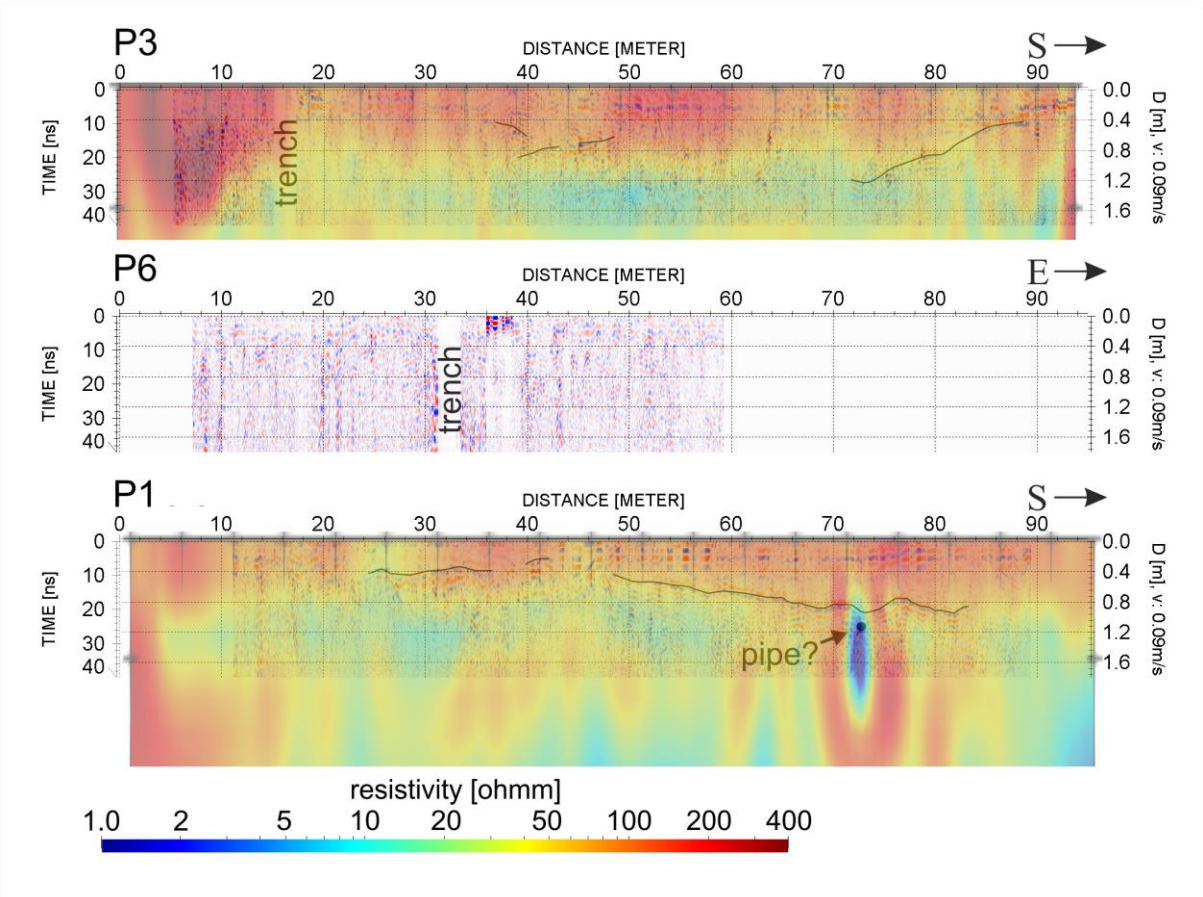

Figure 14: Radargrams overlain by the ERT results. A sharp change in electrical permittivity is indicated by the black line. The presence of the pipe is shown as a hyperbola in the radargram.

Seismic refraction tomography

The seismic refraction data was initially processed with ReflexW from K. Sandmeier. Unfortunately, it turned out that the first arrivals were overlain by the airwave (see Fig. 15). This made it impossible to pick the first arrivals consistently. We therefore decided to quit the refraction processing and use the data only for MASW processing instead.

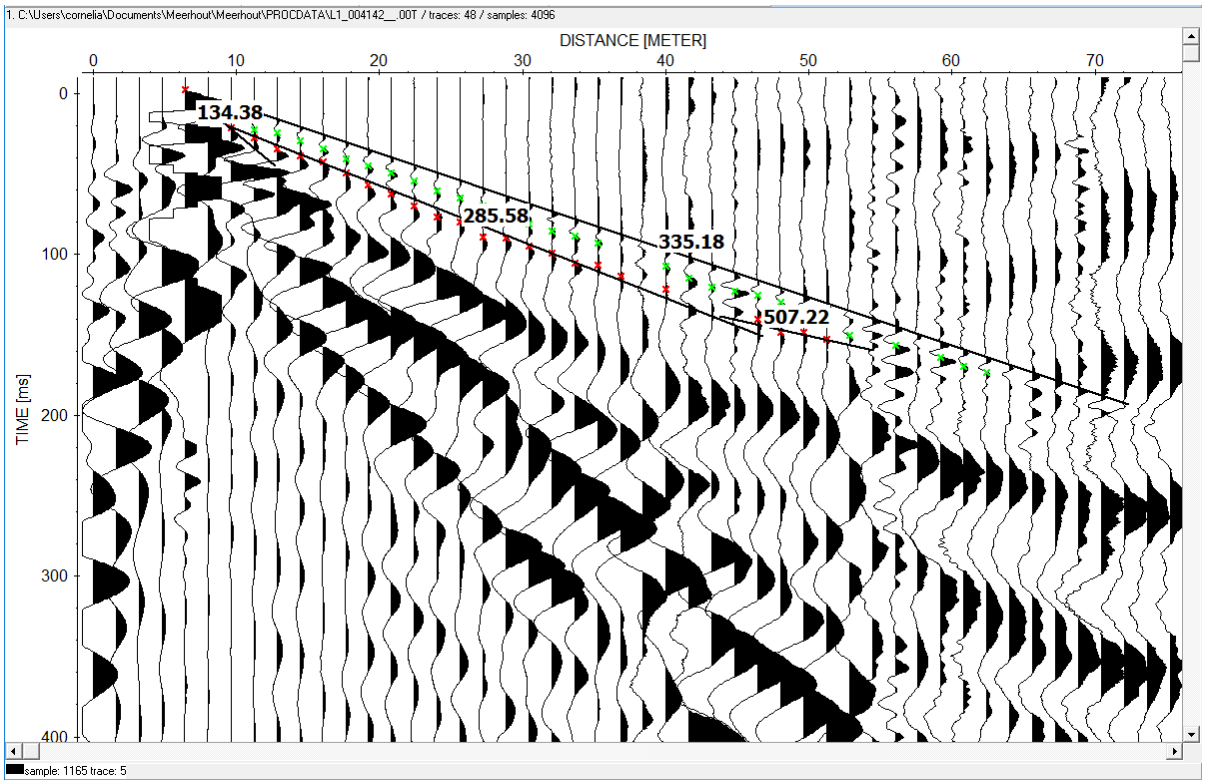

Figure 15: Example seismic shot gather. The airwave with a velocity around 335.18 m/s covers the first arrivals making it difficult to pick the data consistently (i.e. it is unsure whether the red or the green example picks would correspond to the first arrivals).

MASW

The surface wave processing was developed by using three approaches: a standard inversion in GEOPSY, a statistical approach using Bayesian Evidential Learning and an approximated approach using SurfSEIS. The former two were used to estimate the velocity of the waste layer. The latter was used in order to produce depth sections of the shear wave velocity distribution. For all approaches, the analysis of the dispersion curves was not straightforward due to the low velocity of surface waves and superposition of higher modes waves; this was specifically the case for data from the top part of the landfill.

Velocity estimation of the waste layer (inversion and statistical approach):

In a general way, both approaches allowed to estimate the shear wave velocities of the waste layer to be between 100-210 m/s at the northern investigation area 1 and 100-180 m/s at the southern investigation area 2. Figures 16-17 show the results of the inversion and the statistical approach for one source location in different profiles and on both investigation areas. Figure 16 shows one example of velocity estimation in profile 7 (see location in Fig. 2b). For both approaches, the average velocity of the shallow waste layer is between 120 m/s and 140 m/s. Figure 17 shows one example for profile 3 (P3) where the estimated velocity is approximately 120 m/s using both software.

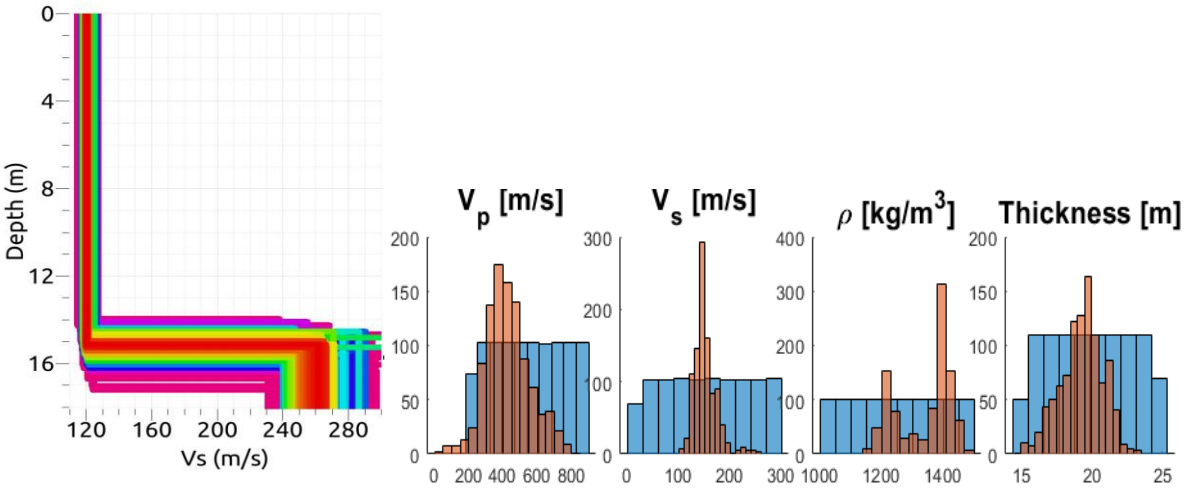

Figure 16: Example of shear wave velocity estimation for one source in seismic profile 7. On the left, the inversion result using GEOPSY and on the right, the statistical approach where blue bars represent a priori information and orange bars are the probability density functions.

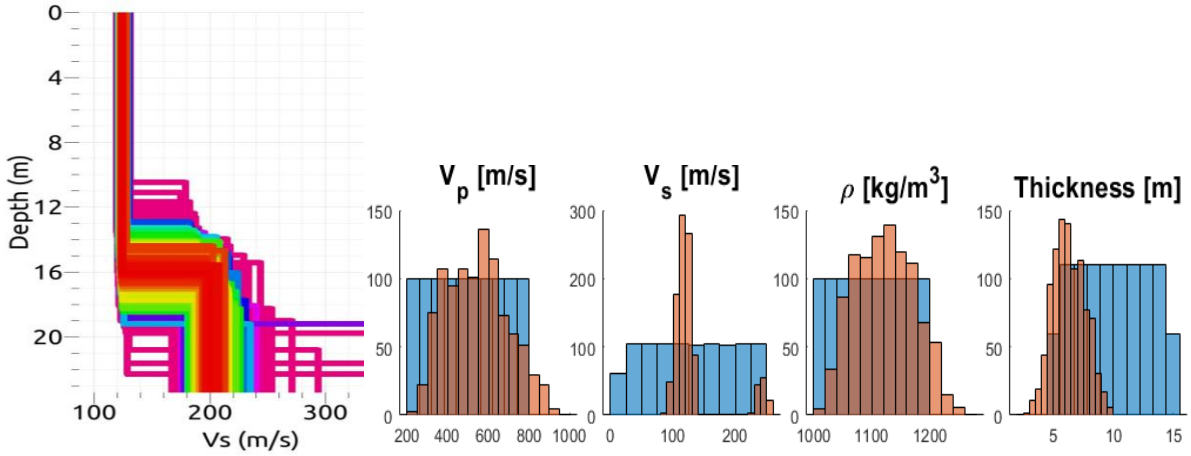

Figure 17: Example of shear wave velocity estimation for one source in seismic profile 3. On the left, the inversion result using GEOPSY and on the right, the statistical approach where blue bars represent a priori information and orange bars are the probability density functions.

For both processing methods, we observed a great variability in the results with minor modifications in the a priori parameters. The estimated depths of the first layer, in some cases did not match with the previously known thickness of the waste; this can be due to the resonance frequency of the geophones or possibly the similarity between the velocities of surface waves in waste and in the underlying medium (alluvial soil). In spite of the challenges of the data processing, a general perspective of the surface wave velocities -at least in the shallower zones- could be estimated and further sampling surveys will be useful to corroborate these results.

Approximation of shear wave velocity depth sections along each profile line:
In order to create shear wave velocity depth sections along each profile line, we used an approximation approach. This included using the software SurfSEIS (Kansas Geological Survey (KGS)) to pick the dispersion curve of each shot record including 12 geophones adjacent to a shot position. Each

picked dispersion curve was then converted to a shear wave velocity (Vs) versus depth profile by approximating the depth of investigation to be equal to one third of the wavelength as follows (Milsom and Eriksen 2011):

$$depth = \frac{Vs}{3\,f} \qquad \text{(with wavelength } \lambda = Vs/f\text{)}.$$

The depth sections were then finally obtained by positioning each Vs versus depth profile at the midpoint of each shot record.

A 3D-view including all depth sections is displayed in Figures 18 and 19. In addition, each profile is shown as a 2D-section in Appendix D allowing a more detailed view and a comparison of the MASW data with the HVSNR results described in the next section. The colour scale is chosen such that velocities below 200 m/s, which are normally related to made ground (waste layer), are green to blue. The higher velocities being indicative for the host formation are coloured in orange to red. In Appendix D, the Vs versus depth profiles of each shot record are superimposed as black lines giving a better indication about gradual or abrupt changes in velocity.

The MASW results on the northern investigation area 1 (Fig. 18 and Appendix D, Fig. 1-4) and the southern investigation area 2 (Fig 19 and Appendix D, Fig. 5-6) show a shallow layer of velocities lower than 200 m/s. This is consistent with the waste layer velocities estimation above. An interesting high velocity anomaly is present at shallow depth in the south-western corner (profiles P1 South and profile P4 West). This might be related to a change locally higher compacted material of the cover layer. The thickness of the low velocity waste layer is thicker on investigation area 2 where it reaches around 15 m. On investigation area 1, the waste thickness is indicated to be around 10 m. However, the transition to higher velocities above 250 m/s, which would be indicative for the host formation, is rather gradual. It is therefore difficult to provide a reliable estimation of the waste thickness. Calibrating the data with ground truth information from the boreholes might later allow to improve this estimation. In addition, ground truth data could be used to improve the starting model for a MASW inversion. Preliminary attempts to invert the picked dispersion curves resulted in a scattered, unrealistic Vs distribution. The reason for this might be the relatively sparse data coverage because the MASW data was extracted from a setup for seismic refraction.

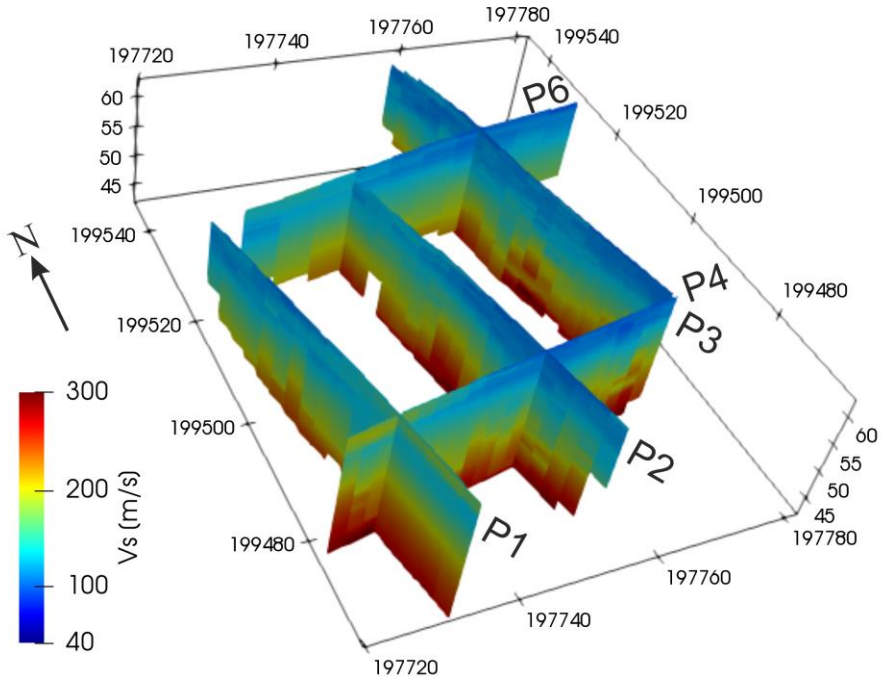

Figure 18: Results of the MASW data from the northern investigation area 1. The results are displayed as approximated shear wave velocity (Vs) depth section.

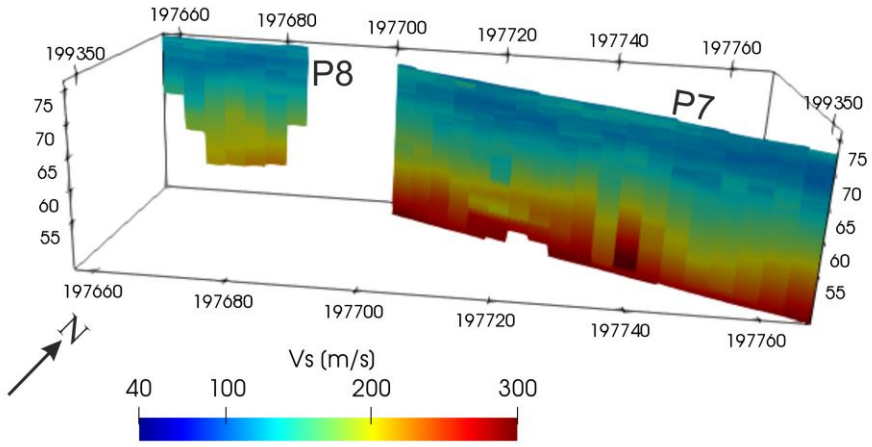

Figure 19: Results of the MASW data from the southern investigation area 2. The results are displayed as approximated shear wave velocity (Vs) depth section.

HVSNR

The technique was popularized by Nakamura (1989) and consists in estimating the resonance frequency of a media using vertical and horizontal Fourier spectrums. First, the acquired data are 3 components seismographs: one vertical (V) and two horizontal (H) (i.e. vertical, north-south and east-west directions) for one recording station along the seismic profile. Then, for each station the following process was done using the software GEOPSY:

1. Selection of the N most stationary windows in the 3 components
2. Computation of Fourier amplitude spectra for each time windows (+ smoothing)
3. Average of horizontal components
4. Computation of N horizontal/vertical components ratios (H/V)
5. Computation of the average H/V ratio

Then the frequency where the higher amplitude of the H/V ratio is shown, corresponds to the resonance frequency f_0 of the underlying media in each recording station (see example in Fig. 20). In most of the recording seismic stations, there were at least two well-defined peaks at two main frequencies although only one at the maximum amplitude.

With the previous results of MASW techniques (S wave velocity β) and the resonance frequency f_0 it is possible to determine the thickness of the first layer H according to:

$$f_0 = \frac{\beta}{4\,H}$$

Based on this, the thickness of the first layer H was calculated for each station along each profile (see Fig. 2b). Figures 21 to 25 show the topography (black line) where the dots represent the seismic stations and the possible delineation of the waste bottom limit or other layers within/below the body waste (red lines). The bottom limit displayed in profiles P1, P2 and P4 is below the thickness of the waste, perhaps to the lack of contrast between the waste and the material buried below it, e.g. sand, clay. In the case of the profile P3, the calculated bottom limit corresponds with the thickness of the waste. In the upper zone of the site, the profile 7 may also display the bottom limit of the waste plus a layer of sand or clay as the limit is below the waste thickness. The results of the short profile P8 are

not shown because of the high level of anthropogenic noise, in this case the resonance frequency originated from the air may overlap with the resonance frequency of the waste bottom limit.

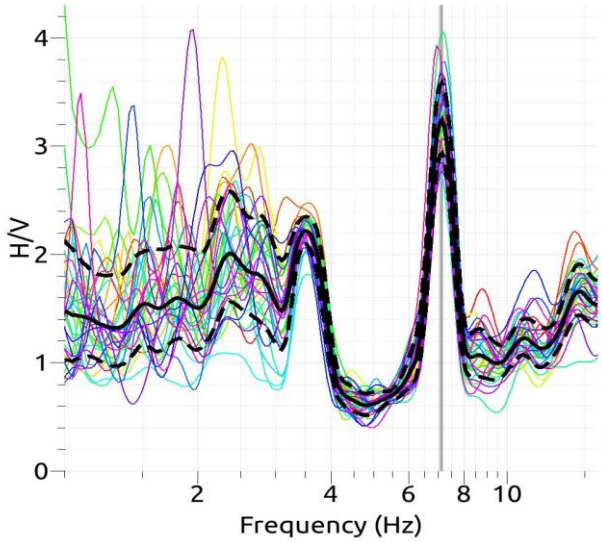

Figure 20: H/V average ratio for one station in profile P3. The grey band indicates the highest H/V value at the resonance frequency $f_0 = 7.13\ Hz$

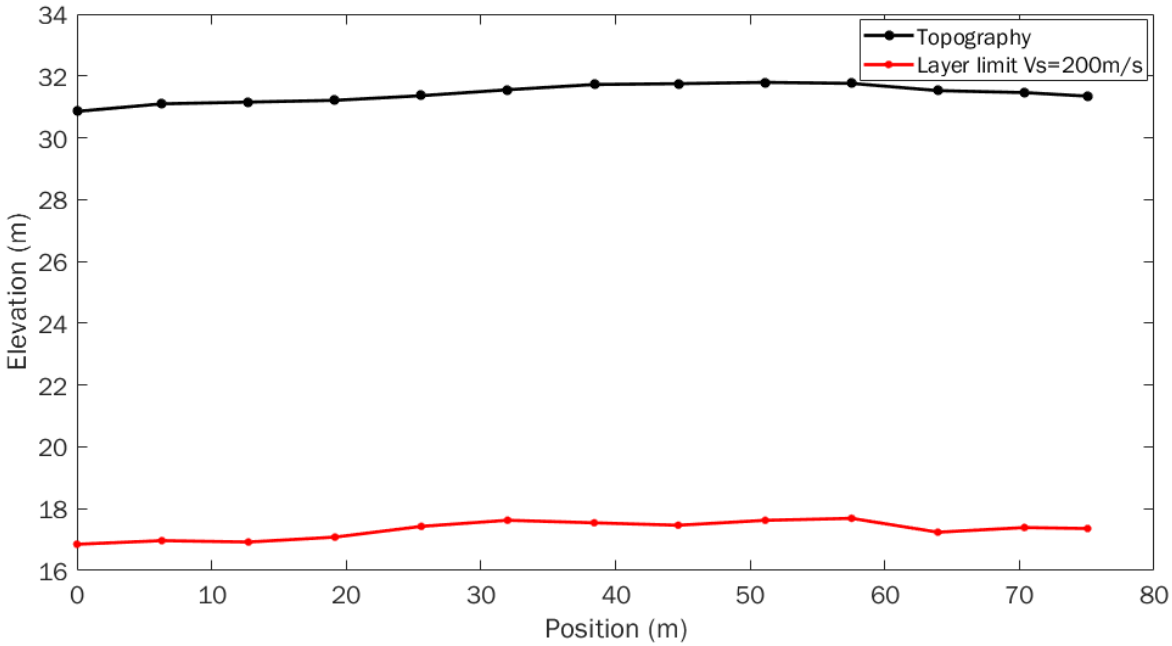

Figure 21: P1 Origin in the northeast of P1 (see Fig. 2b), SE-NW oriented.

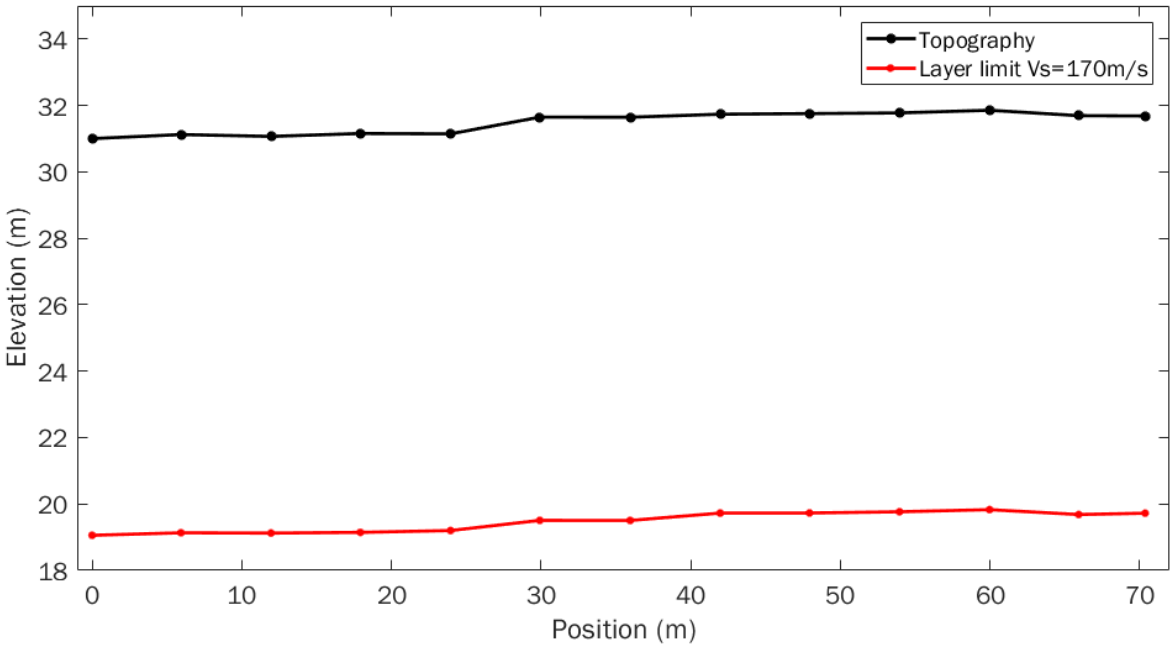

Figure 22: P2, SE-NW oriented

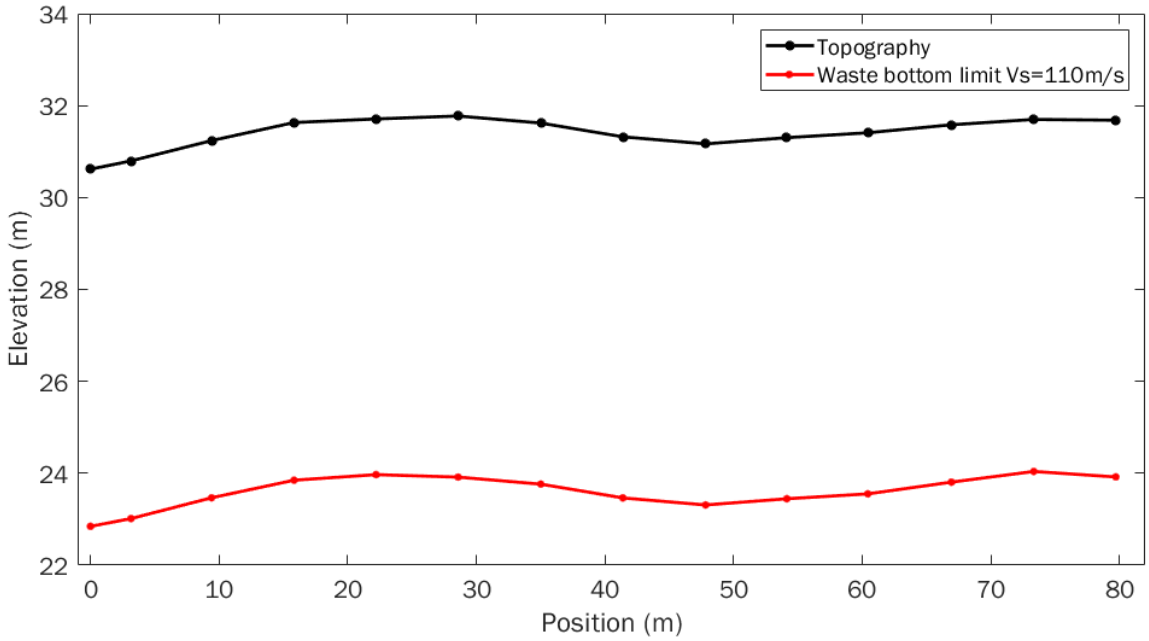

Figure 23: P3, SE-NW oriented

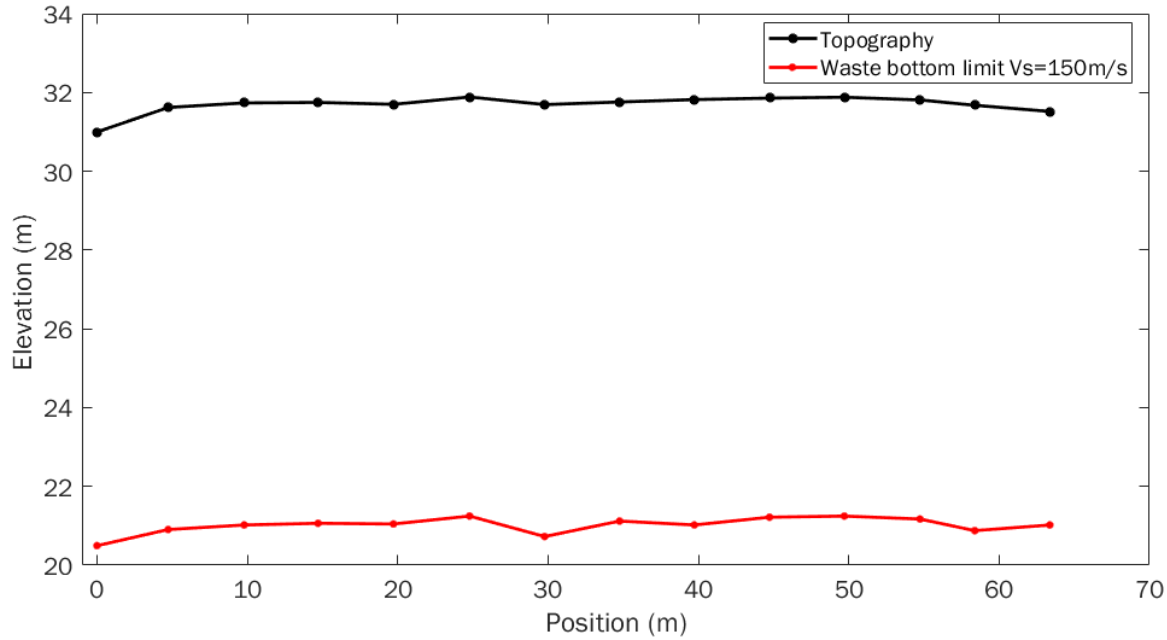

Figure 24: Profile P4 whose origin is in its label of Figure 2Bb, SW-NE oriented

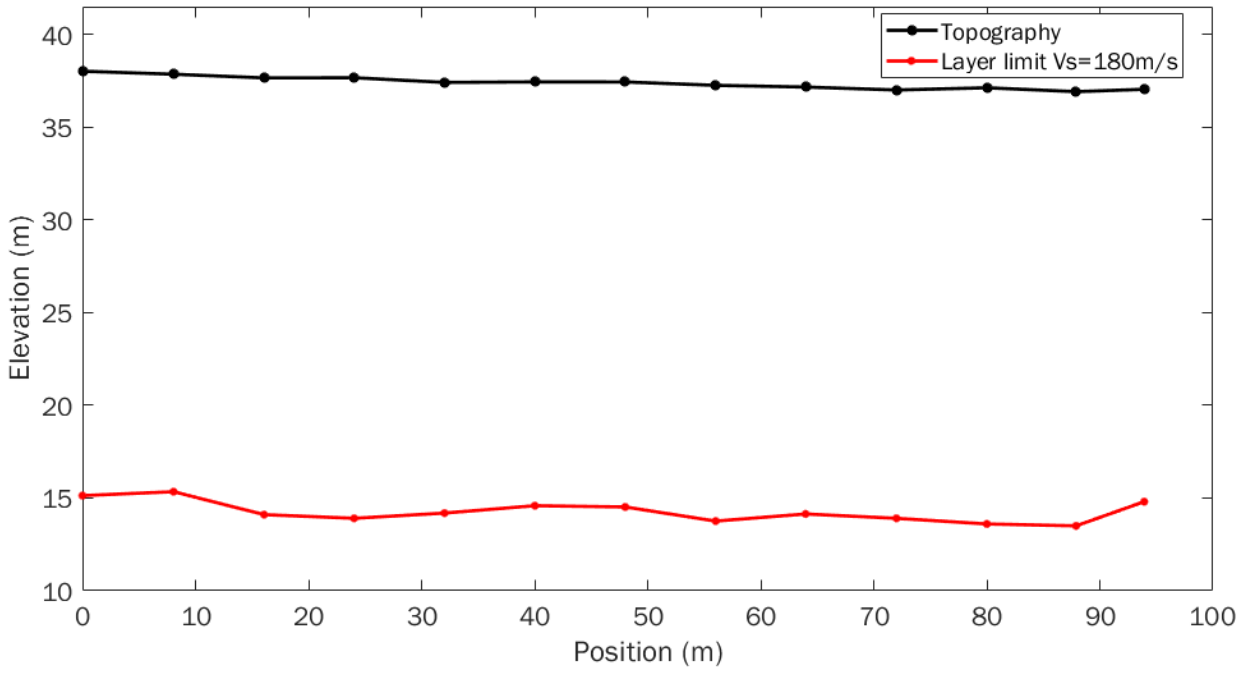

Figure 25: P7 Origin indicated with the P7 label of Fig. 2b, SE-NW oriented.

Conclusions and proposed sampling positions

The geophysical measurements identified several interesting anomalies. In order to verify and calibrate the measurements, we defined the position of several sampling boreholes and a long trench running in East-West direction through the middle of investigation area 1. An initial proposition of sampling locations is displayed as purple dots and a green line in the Figure 26 below and in Figures 4 – 13. The main interest and an explanation for each sampling position is given on the following page.

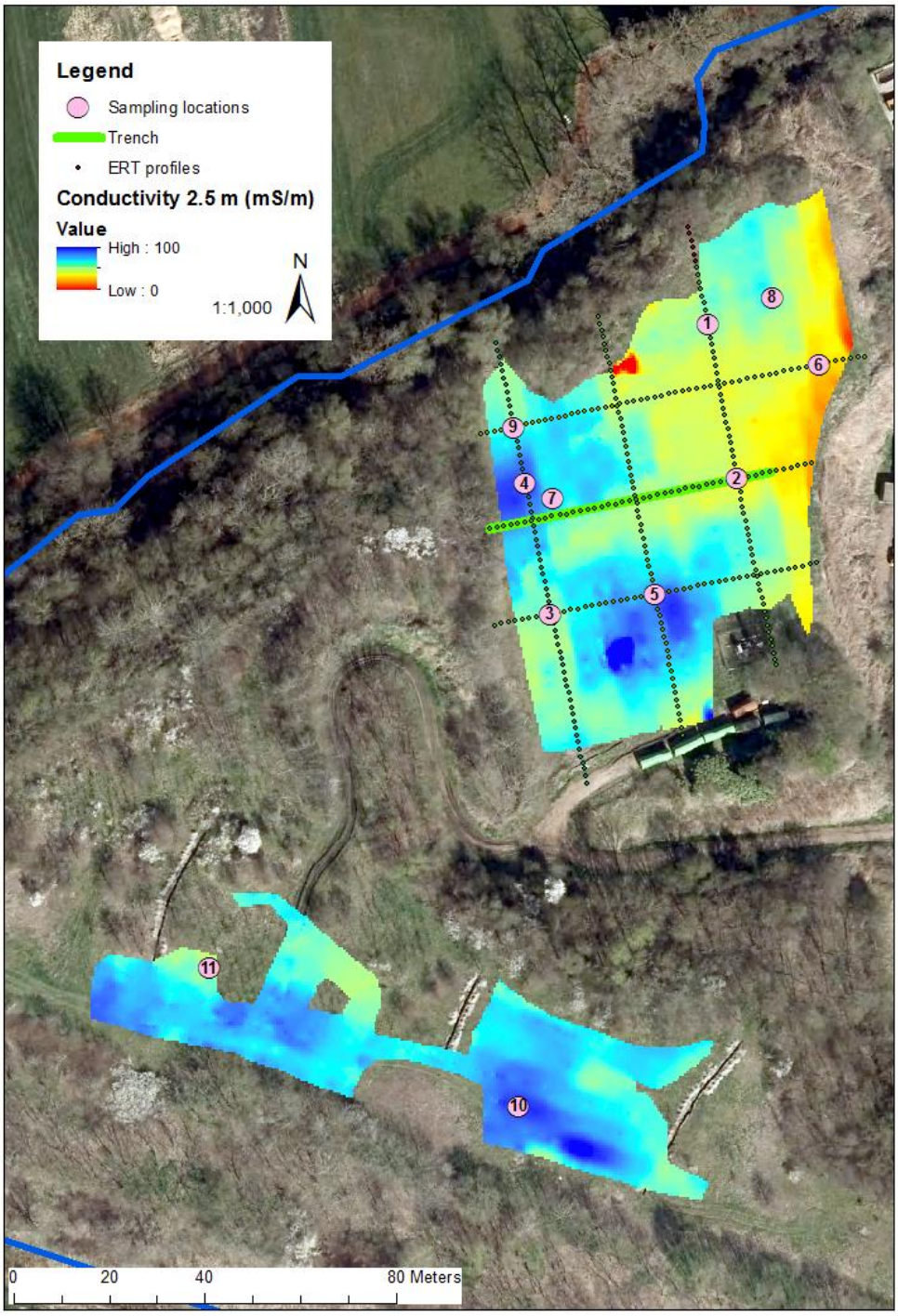

Figure 26: Electrical conductivity map derived from the quadrature-phase data measured with the 4 m antenna and vertical coil alignment

The sampling positions were chosen such that we were able to verify the following discovered anomalies:

Sampling on investigation area 1

- **Borehole Nr. 7:** strong magnetic anomaly indicating a big metallic object.
- **Borehole Nr. 2:** potential earth dam seen in the magnetic and the HVNSR results running in E-W direction through the middle of area 1
- **Borehole Nr. 1, 8, 6:** area with highly perturbed value in the vertical gradient (magnetics) and magnetic susceptibility data (EM).
- **Borehole Nr. 2 and 6:** low conductivity anomaly in the EM data
- **Borehole Nr. 4 and 5:** high conductivity anomaly in the EM data
- **Borehole Nr. 1, 3, 4 and 9:** anomalies in the ERT and IP data at depth
- **Borehole Nr. 2, 3, 6 and trench:** validation of the shallow layering structure seen in the resistivity and IP data
- **Borehole Nr. 3:** validation of the layer with a sharp change in electrical permitting seen in the GPR radargrams

Sampling on investigation area 2:

- **Borehole Nr. 10 and 11:** contrast in the total magnetic field and the conductivity (EM)
- **Borehole Nr. 10:** anomaly in the magnetic susceptibility data (EM)

All the proposed locations could also help verifying the waste bottom limit derived from the HVNSR measurements.

References

Carlson, N. R., Hare, J.L., Zonge, K.L. (2001). "Buried landfill delineation with induced polarization: Progress and problems, in: Symposium on the Application of Geophysics to Engineering and Environmental Problems (SAGEEP).".

Dumont, G., T. Robert, N. Marck and F. Nguyen (2017). "Assessment of multiple geophysical techniques for the characterization of municipal waste deposit sites." *Journal of Applied Geophysics* **145**: 74-83.

Knödel, K., G. Lange and H.-J. Voigt (2007). Environmental geology handbook of field methods and case studies. Berlin, Springer.

Loke, M. H. (2016). "Tutorial : 2-D and 3-D electrical imaging surveys."

Milsom, J. and A. Eriksen (2011). Field geophysics. Hoboken, NJ, Wiley.

Michel, H., Hermans, T., & Nguyen, F. (2019). 1D geological modeling of the subsurface from geophysical data with Bayesian Evidential Learning. Paper presented at the EGU General Assembly 2019 Vienna.

Park, C. B., R. D. Miller and J. H. Xia (1999). "Multichannel analysis of surface waves." *Geophysics* **64**(3): 800-808.

Roberts, R., Hinze, W., Leap, D. (1990b). "Data Enhancement Procedures on Magnetic Data from Landfill Investigations." Geotechnical and Environmental Geophysics, Investigations in Geophysics. S*ociety of Exploration Geophysicists*: 261–266.

Roberts, R., Hinze,W., Leap, D. (1990a). "Application of the Gravity Method to Investigation of a Landfill in the Glaciated Midcontinent, U.S.A." Geotechnical and Environmental Geophysics, Investigations in Geophysics. *Society of Exploration Geophysicists*: 253–260.

Thierry, B., Weller, A., Schleifer, N., Westphal, T. (2001). "Polarisation effects of wood. Presented at the Proceedings of 7th Meeting of EEGS-ES, Birmingham.".

Contact

Feel free to contact us.

Local contact details:

BELGIUM	ATRASOL	renaud.derijdt@atrasol.eu
	Cleantech Flanders / VITO	alain.ducheyne@vito.be
	OVAM	ewille@ovam.be
	SPAQuE	c.neculau@spaque.be
	Université de Liège	f.nguyen@ulg.ac.be
FRANCE	SAS Les Champs Jouault	champsjouault@gmail.com
GERMANY	BAV	pbv@bavmail.de
THE UK	NERC	jecha@bgs.ac.uk

Coordination office:

BELGIUM	SPAQuE Boulevard Maurice Destenay, 13 4000 Liège	c.neculau@spaque.be

Appendix A

Meerhout measurement parameters							
Mapping	**Profile**	**line spacing [m]**	**inline resolution**	**depth levels**	**system**	**positioning**	**other specifications**
Magnetics	grid1 & 2	2	1 meas. per second	undefined	G-858 (Geometrics)	synchronized GPS (no RTK)	
EM 2m antenna	grid1 & 2	2	1 meas. per second	1.2m & 3m	DUALEM-4	synchronized GPS (no RTK)	
EM 4m antenna	grid1 & 2	4		2.5m & 6m			
2D Profiles	**Profile**	**amount electrodes/ geophones**	**electrode/ geophone spacing [m]**	**amount recorded data**	**system**		**other specifications**
ERT/IP	P1	64	1.5	1793 reciprocal pairs	SuperSting R8/IP	each electrode surveyed with RTK corrected GPS	chargeability time window: 1.2 s
	P2	61		1620 reciprocal pairs			chargeability time window: 0.6 s
	P3	64		1780 reciprocal pairs			
	P4	47		1103 reciprocal pairs			
	P5	47		1103 reciprocal pairs			
	P6	56		1460 reciprocal pairs			
SRT/MASW	P1	45	1.6	31 shot gathers	ABEM	each electrode surveyed with RTK corrected GPS	alternated 4.5Hz & 10Hz geophones
	P2		1.5	31 shot gathers			10Hz geophones
	P3		1.6	31 shot gathers			10Hz geophones
	P4		1.25	28 shot gathers			alternated 4.5Hz & 10Hz geophones
	P6		1.5	15 shot gathers			alternated 4.5Hz & 10Hz geophones
	P7		2	31 shot gathers			10Hz geophones
	P8	24	2	19 shot gathers			two repeat sets with 4.5Hz and 10Hz geophones
GPR	P1		continuous measurement along profile (sampling frequency: 250MHz)	-	PulsEkko Noggin		250 MHz antenna
	P3						
	P7						
HVSNR	P1	13	6.4	13-3D noise seismograms	LE-3D/5s MkIII and LE-3Dlite MkIII	each station surveyed with RTK corrected GPS	15 minutes recording per seismic station
	P2	12	6	12-3D noise seismograms			
	P3	14	6.4	14-3D noise seismograms			
	P4	14	5	14-3D noise seismograms			
	P7	13	8	13-3D noise seismograms			
	P8	7	8	7-3D noise seismograms			

Appendix B

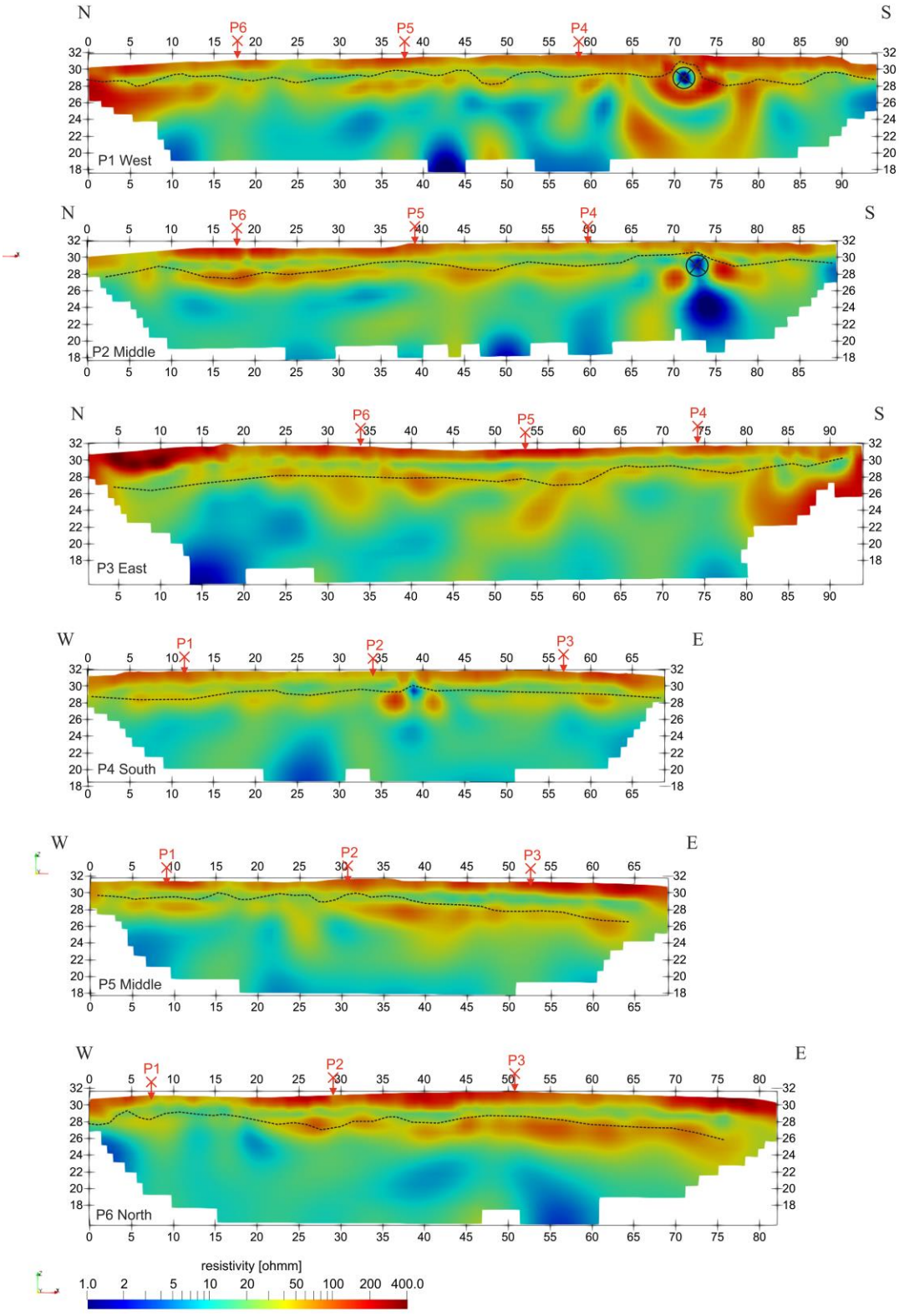

Electrical restivity profiles. The black dotted line indicates the bottom of the layer with small chargeabiliry seen in Appendix C. The circle indicates the position a metalic tube.

Appendix C

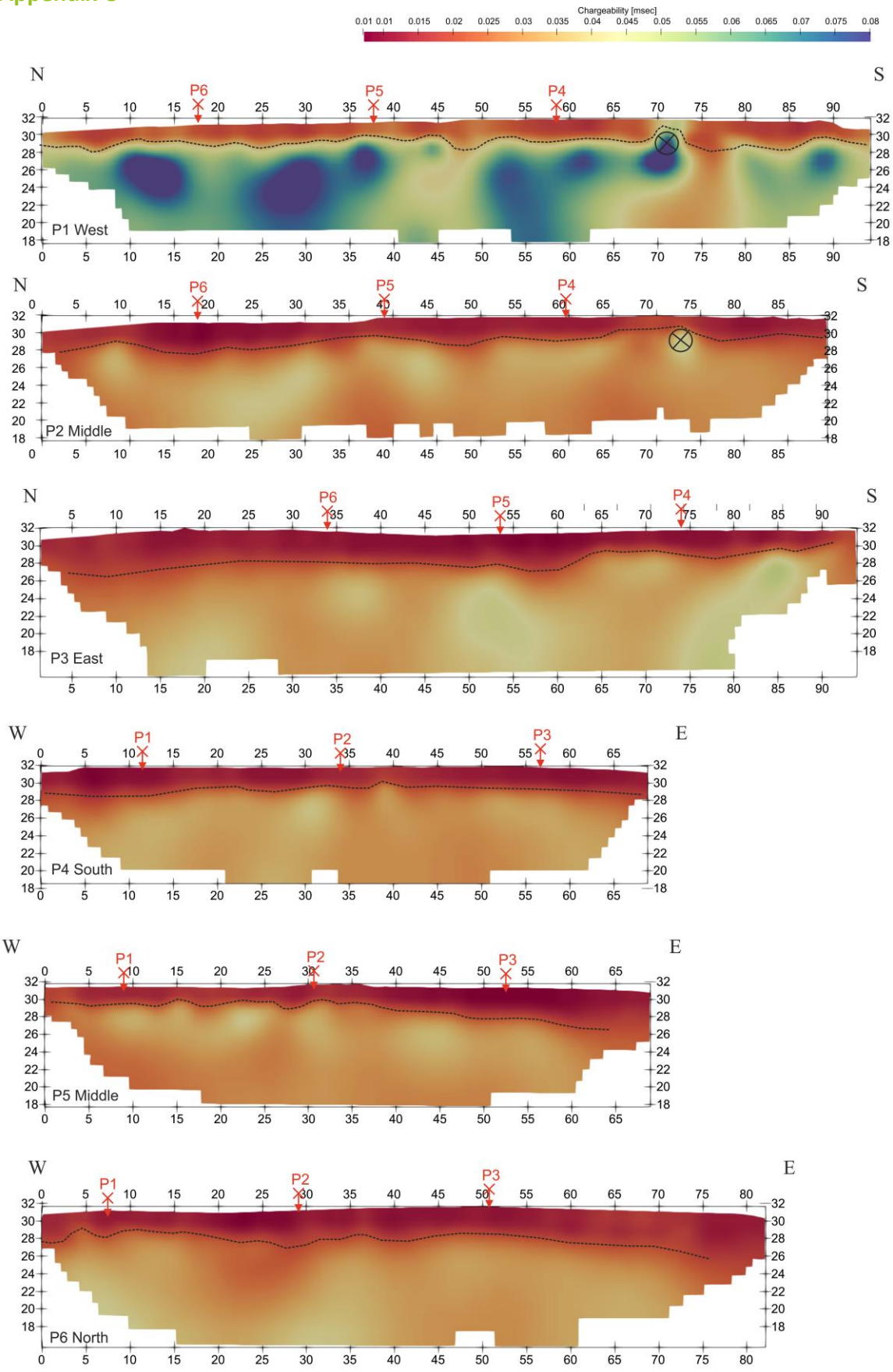

Chargeability profiles. The black dotted line indicates the bottom of the layer with small chargeabiliry. The black circle indicates the position of a metallic tube

Appendix D

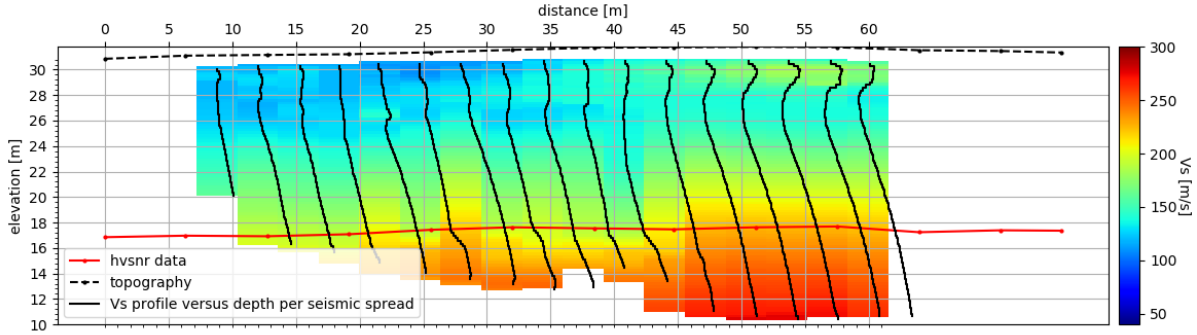

Figure 1: MASW results of profile P1 (N-S oriented) displayed as shear wave velocity depth section. As a comparison, the results of the HVNSR data is plotted onto it (red line).

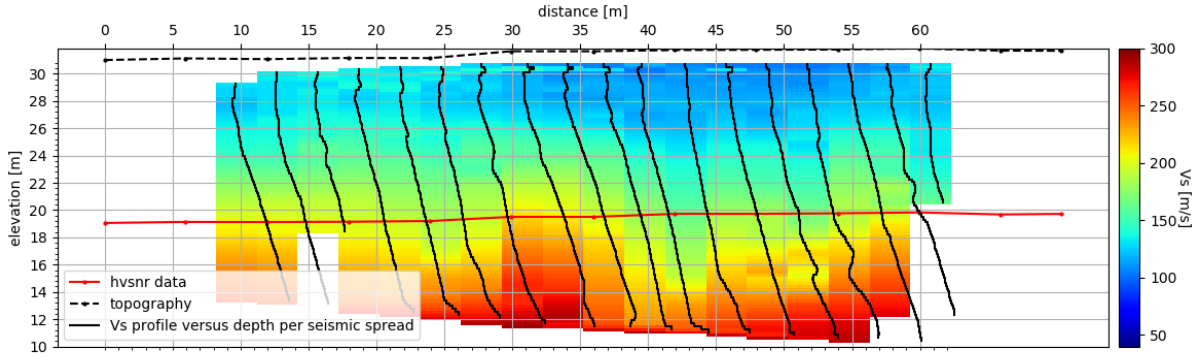

Figure 2: MASW results of profile P2 (N-S oriented) displayed as shear wave velocity depth section. As a comparison, the results of the HVNSR data is plotted onto it (red line).

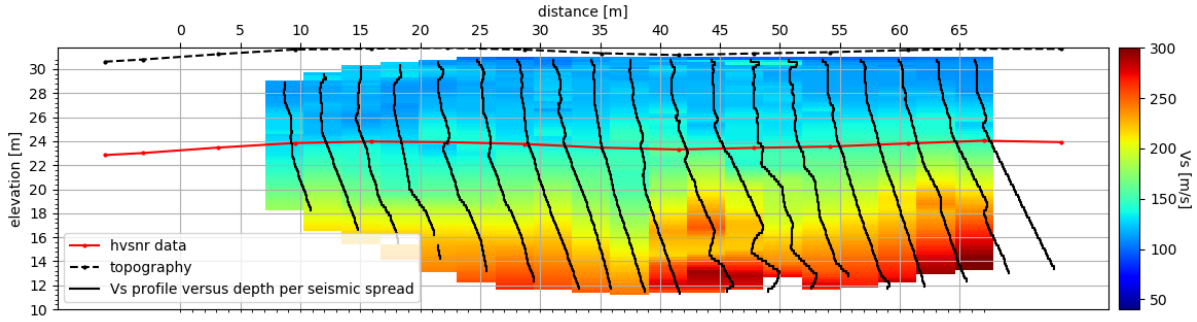

Figure 3: MASW results of profile P3 (N-S oriented) displayed as shear wave velocity depth section. As a comparison, the results of the HVNSR data is plotted onto it (red line).

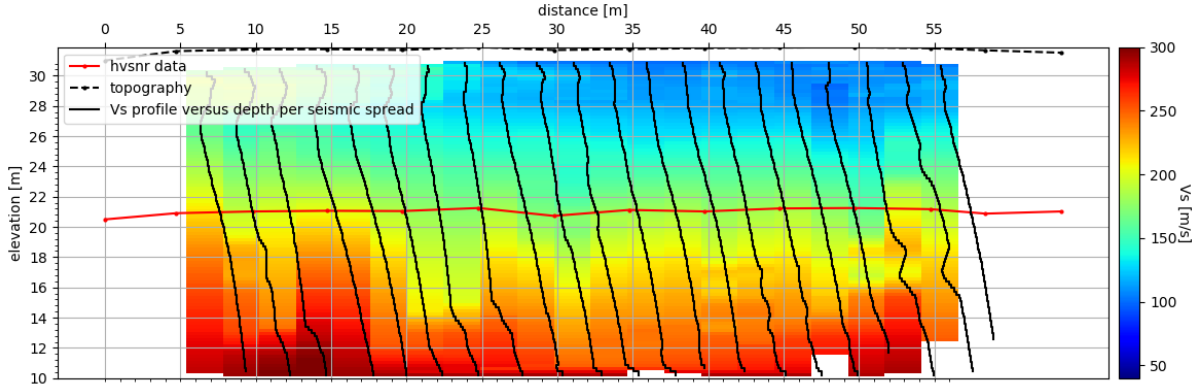

Figure 4: MASW results of profile P4 (W-E oriented) displayed as shear wave velocity depth section. As a comparison, the results of the HVNSR data is plotted onto it (red line).

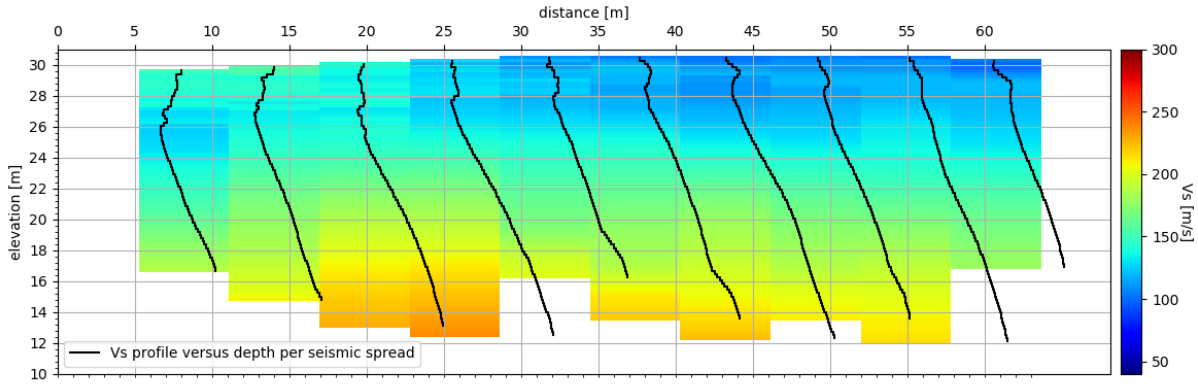

Figure 5: MASW results of profile P6 (W-E oriented) displayed as shear wave velocity depth section. As a comparison, the results of the HVNSR data is plotted onto it (red line).

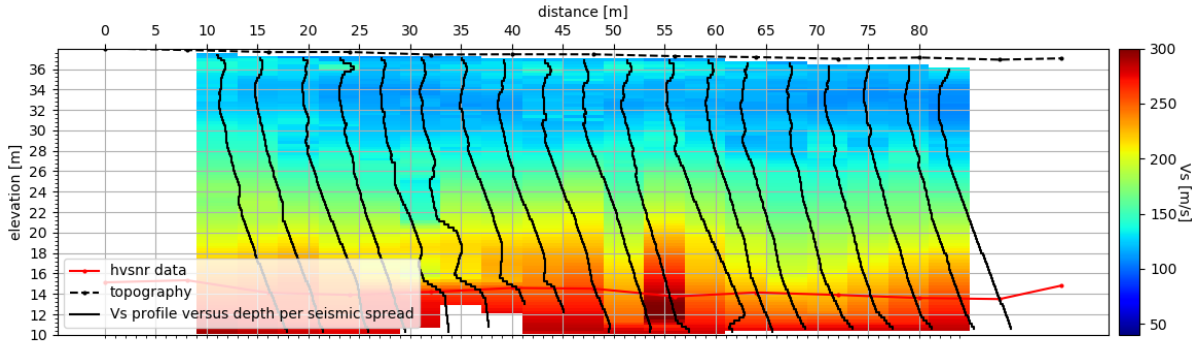

Figure 6: MASW results of profile P7 (W-E oriented) displayed as shear wave velocity depth section. As a comparison, the results of the HVNSR data is plotted onto it (red line).

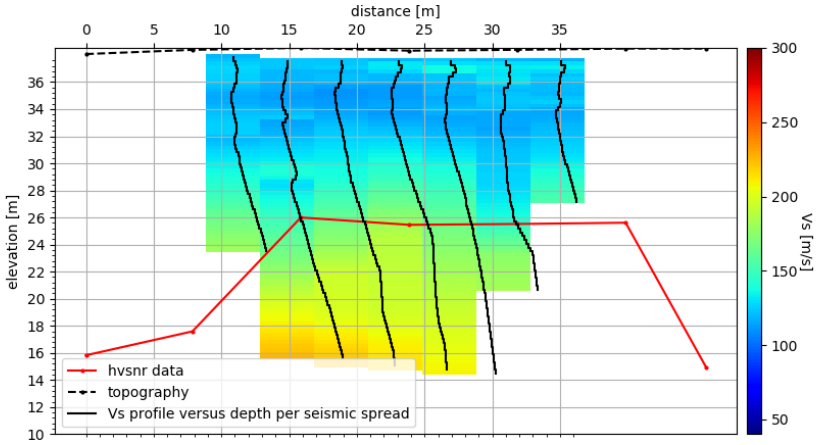

Figure 7: MASW results of profile P8 (E-W oriented) displayed as shear wave velocity depth section. As a comparison, the results of the HVNSR data is plotted onto it (red line).